



Full length article

# In vivo stiffness measurement of epidermis, dermis, and hypodermis using broadband Rayleigh-wave optical coherence elastography

Xu Feng<sup>a,c,1</sup>, Guo-Yang Li<sup>a,c,1</sup>, Antoine Ramier<sup>a,b</sup>, Amira M. Eltony<sup>a,c</sup>, Seok-Hyun Yun<sup>a,b,c,\*</sup>

<sup>a</sup> Harvard Medical School and Wellman Center for Photomedicine, Massachusetts General Hospital, Boston, MA 02114, United States

<sup>b</sup> Harvard-MIT Division of Health Sciences and Technology, Cambridge, MA 02139, United States

<sup>c</sup> Department of Dermatology, Massachusetts General Hospital, Boston, MA 02114, United States

## ARTICLE INFO

### Article history:

Received 24 January 2022

Revised 14 April 2022

Accepted 19 April 2022

Available online 22 April 2022

### Keywords:

Skin

Layered tissues

Optical coherence elastography

Rayleigh surface wave

Stiffness

## ABSTRACT

Traveling-wave optical coherence elastography (OCE) is a promising technique to measure the stiffness of biological tissues. While OCE has been applied to relatively homogeneous samples, tissues with significantly varying elasticity through depth pose a challenge, requiring depth-resolved measurement with sufficient resolution and accuracy. Here, we develop a broadband Rayleigh-wave OCE technique capable of measuring the elastic moduli of the 3 major skin layers (epidermis, dermis, and hypodermis) reliably by analyzing the dispersion of leaky Rayleigh surface waves over a wide frequency range of 0.1–10 kHz. We show that a previously unexplored, high frequency range of 4–10 kHz is critical to resolve the thin epidermis, while a low frequency range of 0.2–1 kHz is adequate to probe the dermis and deeper hypodermis. We develop a dual bilayer-based inverse model to determine the elastic moduli in all 3 layers and verify its high accuracy with finite element analysis and skin-mimicking phantoms. Finally, the technique is applied to measure the forearm skin of healthy volunteers. The Young's modulus of the epidermis (including the stratum corneum) is measured to be  $\sim 4$  MPa at 4–10 kHz, whereas Young's moduli of the dermis and hypodermis are about 40 and 15 kPa, respectively, at 0.2–1 kHz. Besides dermatologic applications, this method may be useful for the mechanical analysis of various other layered tissues with sub-mm depth resolution.

### Statement of Significance

To our knowledge, this is the first study that resolves the stiffness of the thin epidermis from the dermis and hypodermis, made possible by using high-frequency (4 – 10 kHz) elastic waves and optical coherence elastography. Beyond the skin, this technique may be useful for mechanical characterizations of various layered biomaterials and tissues.

© 2022 Acta Materialia Inc. Published by Elsevier Ltd. All rights reserved.

## 1. Introduction

The skin is a layered tissue characterized by 3 major layers, namely, the epidermis, dermis, and hypodermis. Each layer plays an important role in maintaining the structural integrity and pathophysiological functions of the skin. The epidermis is the outermost protective layer ( $\sim 100$   $\mu\text{m}$  in most body sites), consisting of the stratum corneum (SC) and viable epidermis [1, 2]. The dermis is the middle layer with a typical thickness of  $\sim 1$  mm [2], providing nourishment and mechanical support for the epidermis [3]. The hypodermis is the softest layer with a thickness of a few mm.

Characterizing the biomechanical properties of individual skin layers in vivo is important for understanding the aging process [4], as well as the mechanisms of other dermatological conditions such as scarring [5], skin cancer [6], and inflammatory reactions with edema or fibrosis [7].

Several methods have been developed to measure skin elasticity in vivo. Mechanical techniques such as tonometry, indentation, suction, torsion and twisting are useful to measure the various mechanical properties of the skin as a whole, but cannot resolve the individual skin layers [8] and, when applied in vivo, are subject to significant variability dependent on experimental conditions [9]. Elastography based on different imaging modalities, such as ultrasound and optical coherence tomography (OCT), have been applied to characterize the layered mechanical properties of the skin. Ultrasound elastography has been used to resolve the Young's mod-

\* Corresponding author.

E-mail address: [syun@hms.harvard.edu](mailto:syun@hms.harvard.edu) (S.-H. Yun).

<sup>1</sup> Co-first authors with equal contribution.

ulus in the dermis and hypodermis [10–13]. However, the resolution (~300 μm) of ultrasound is insufficient to resolve the epidermis. Optical coherence elastography (OCE) takes advantage of the high imaging resolution (~ 10 μm) of OCT and has been applied to characterizing the skin [14–19]. Compression-based OCE methods measure static strains in the skin layers under a bulk compressional force [6, 19] but cannot directly quantify the Young’s moduli of individual skin layers [20].

Optical visualization and measurement of mechanical waves is the most studied approach in OCE, which enables quantitative characterization of elasticity with spatial resolution approximately proportional to the wavelength or spatial pulse width of the mechanical wave [21, 22]. Various wave-based OCE techniques have been used to characterize layered tissues and phantoms in previous studies [23–25]. In particular, Rayleigh surface wave OCE offers a promising approach to obtain depth-resolved information as surface waves can be readily excited and measured at the skin’s surface without the constraint of imaging depth. For skin tissues, the Rayleigh waves are typically leaky waves with both dissipative and dispersive losses along the surface. The amplitude of surface waves decays exponentially with depth. At any transverse location, the 50%-energy penetration depth is about a half wavelength [26]. Considering the typical thicknesses of human epidermis and dermis and the bulk shear wave velocity of ~ 4 m/s in the dermis, we find that the Rayleigh wave at 3 kHz predominantly occupies the dermis, while the Rayleigh wave at 10 kHz has ~ 50% energy in the thin epidermis. It is evident that high-frequency measurement is essential to resolve the elasticity of individual skin layers.

Several approaches for excitation of Rayleigh waves in skin have been investigated. Air puff excitation, which has a typical bandwidth of a few hundred Hz, has been applied to differentiating macroscopic lesions such as systemic sclerosis [18], but cannot resolve individual skin layers due to the long wavelength (~ 10 mm at 400 Hz). Air-coupled acoustic radiation force excitation has recently been developed to measure skin anisotropy in vivo with frequency up to 4 kHz [16]. Zhou et al. [17] measured Rayleigh waves of frequency < 4 kHz in human skin and developed a weighted-average velocity inversion model to estimate the depth profile of elasticity. However, the lack of sufficient high frequency content obscured features in the dispersion curves, resulting in poor reliability for resolving individual skin layers. In our previous work, we used piezoelectric actuated excitation to generate waves with frequencies up to 16 kHz for Rayleigh-wave OCE in the cornea [27, 28].

Here, we demonstrate broadband OCE measurement (0.1–10 kHz) for in vivo quantification of skin elasticity. This study shows, for the first time to our knowledge, the critical benefit of high frequency waves (4–10 kHz) for differentiating the thin epidermal layer from the thicker and softer dermis and hypodermis. The OCE system used has been optimized for the generation and detection of high-frequency waves [27, 28]. We observe feature-rich dispersion curves for human skin and establish a dual bilayer-based model to resolve the distinct stiffnesses of the epidermis, dermis, and hypodermis from the measured dispersion data using simple analytic fitting. We validate this method by finite element analysis (FEA) and tissue phantom experiments and then apply it to human forearm skin in vivo.

## 2. The acoustoelastic model of skin tissues

### 2.1. A bilayer model and key frequencies

The frequency dependent penetration of Rayleigh waves in layered structures has been well recognized, and a number of algorithms have been developed to calculate shear or Young’s moduli of 2 layers and, in some cases, 3 layers from the frequency-

dependent wave velocity (dispersion) curves [17, 29–31]. Access to high-frequency waves (> 4 kHz) should enable inverse calculation for 3 layers with improved global fitting accuracy. However, we have reasoned that a simpler algorithm would be possible considering the differences in the thickness and the bulk wave speed in different skin layers. To explore this, we first consider a bilayer model, as illustrated in Fig. 1(a). This model assumes the layers are elastic, linear, and isotropic. The structure consists of a top layer with a thickness  $h$  and Young’s modulus  $E_1$  (material 1) and a semi-infinite substrate with Young’s modulus  $E_2$  (material 2). We consider the case of stiff layer on soft substrate, that is,  $E_1 > E_2$ . Each material supports bulk transverse shear waves with velocity  $v_{ti} = \sqrt{E_i/(3\rho_i)}$  where  $\rho_i$  is the mass density and subscript  $i$  (=1 or 2) denotes material. The derivation of the dispersion relation for surface waves in the bilayer structure can be found in the literature [13], and a summary is provided in Appendix A. The dispersion relation of the Rayleigh wave speed  $v$  can be described as  $v = v(h, E_1, E_2; f)$ ,  $f$  denotes the wave frequency, and  $h, E_1$ , and  $E_2$  are the three input variables. Other parameters are treated as constants, i.e., Poisson ratio and the density for individual skin layer is assumed to be 0.4999 and 1 g/cm<sup>3</sup>, respectively.

Fig. 1(b) depicts the general dispersion curve of the Rayleigh surface wave. The phase velocity transitions from a low wave speed at  $f \rightarrow 0$  to a high wave speed at  $f \rightarrow +\infty$ . In fact, when  $f \rightarrow 0$  the wave speed  $v_2^{(R)}$  is equal to the Rayleigh (R) surface wave speed [32] of the substrate material:  $v_2^{(R)} \approx 0.955 v_{t2}$ . The phase velocity then increases slowly to  $v_{t2}$  at a critical frequency  $f_2$ , at which the dispersion curve is divided into a nonleaky branch and a leaky branch [33]. It can be shown that  $f_2 \approx \frac{v_{t2}}{6.7 r_{12}^{1/2} h}$ , where  $r_{12} = E_1/E_2$  is the stiffness ratio of the two materials [33]. Beyond this critical point, the wave becomes a leaky surface wave as its phase velocity is greater than the bulk wave speed  $v_{t2}$  of the substrate material, and the leaky wave speed increases rapidly with frequency. When  $f \rightarrow +\infty$  the phase velocity reaches a plateau at  $v_1^{(R)} \approx 0.955 v_{t1}$ , the Rayleigh wave speed of material 1. (Another adiabatic solution exists as the Stoneley interface wave between the two layers, but this wave is ignored as it is not a surface wave.) Approximately, the plateau is reached at a frequency  $f_1 \approx \frac{v_{t1}}{h}$ . We introduce an intermediate frequency  $f_{12} = \sqrt{f_1 f_2}$ , at which the velocity is approximately the average of the two bulk shear velocities,  $(v_{t1} + v_{t2})/2$ . We find  $f_{12} = \frac{v_{t2}}{2.6 h}$ , independent of the stiffness ratio.

### 2.2. The skin model and key frequency ranges

Our main insight is that the 3-layer skin may be decomposed into two bilayer models, the D-H bilayer, as depicted in Fig. 1(d), and the E-D bilayer, as shown in Fig. 1(e), depending on the frequency range. In the lower frequency range, the skin can be modeled as a D-H bilayer: the top layer is the dermis (D), and the hypodermis (H) serves as the substrate. The contribution of the epidermis (E) layer to the Rayleigh surface wave speed can be incorporated by using an equivalent thickness for the dermis,  $\bar{h}_D = \bar{h}_D(h_D, h_E, \frac{E_E}{E_D})$ , where  $h_D$  and  $E_D$ , and  $h_E$  and  $E_E$  are the thickness and Young’s modulus of dermis and epidermis, respectively. We derive  $\bar{h}_D$  by considering the equivalent bending stiffness of the epidermis and dermis in the low frequency range. The result is (see Appendix B):

$$\bar{h}_D \approx h_D \left[ \left( 1 + \frac{4E_E h_E}{E_D h_D} + \frac{6E_E h_E^2}{E_D h_D^2} \right) / \left( 1 + \frac{E_E h_E}{E_D h_D} \right) \right]^{1/3} \quad (1)$$

For typical skin tissues,  $\bar{h}_D$  is 1.5 to 1.7 times  $h_D$ .

In the higher frequency range, the skin can be modeled as an E-D bilayer: the top layer is the epidermis, and the dermis serves as the substrate. In this case, the hypodermis is ignored because the

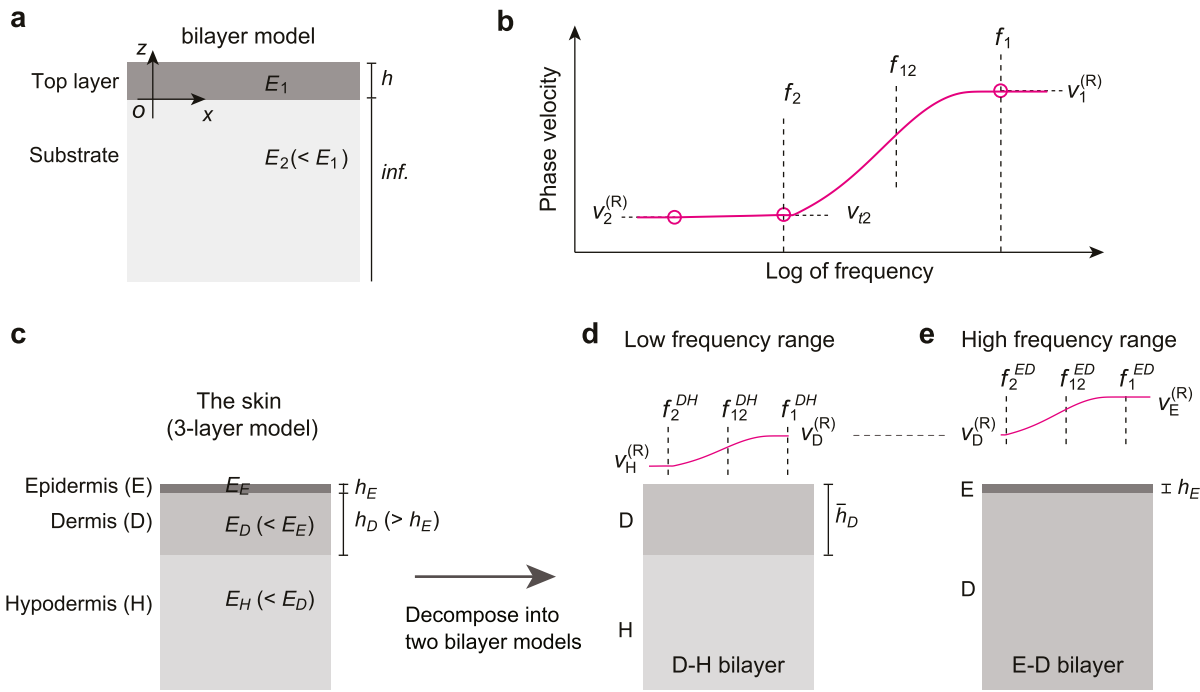


**Fig. 1.** The bilayer models. (a) A basic bilayer model consisting of a top layer with thickness  $h$  and a semi-finite substrate.  $E_1$  and  $E_2$  are the Young's moduli of the top layer and the substrate, respectively, and  $E_2 < E_1$ . (b) A general dispersion relation of the Rayleigh surface wave in the bilayer model. The dispersion curve is divided into two branches at the transverse wave speed of the substrate ( $v_{12}$ ). (c) The 3-layer skin model.  $h_E$  and  $h_D$  are the thickness of the epidermis and dermis, and  $E_E, E_D$  and  $E_H$  are the Young's moduli of the epidermis, dermis, and hypodermis, respectively. (d) The D-H bilayer model in the low frequency range.  $\bar{h}_D$  is an equivalent thickness of the dermis. (e) The E-D bilayer model in the high frequency range. Detailed explanation of the parameters in (d) and (e) can be found in Section 2.2.

**Table 1**

**Typical values of the characteristic frequencies.** For sample 1:  $E_E=1500$  kPa,  $E_D=48$  kPa,  $E_H=6.8$  kPa,  $h_E=80$   $\mu\text{m}$ ,  $h_D=1$  mm, and  $\bar{h}_D=1.5$  mm. For sample 2:  $E_E=4570$  kPa,  $E_D=52$  kPa,  $E_H=18$  kPa,  $h_E=80$   $\mu\text{m}$ ,  $h_D=1$  mm, and  $\bar{h}_D=1.6$  mm.  $v_{iH}$ ,  $v_{iD}$ , and  $v_{iE}$  are the bulk shear wave velocities of the hypodermis, dermis, and epidermis, respectively.  $r_{DH} = \frac{E_D}{E_H}$ ,  $r_{ED} = \frac{E_E}{E_D}$ . The parameters of sample 1 were chosen based on previous literature [13, 17] and are used for the numerical simulation in Fig. 3. The parameters of sample 2 were obtained from the forearm skin of a human (subject #1).

|          | $f_2^{DH}$                        | $f_1^{DH}$           | $f_2^{ED}$                        | $f_{12}^{ED}$            | $f_1^{ED}$           |
|----------|-----------------------------------|----------------------|-----------------------------------|--------------------------|----------------------|
| Formula  | $\frac{v_{iH}}{6.7 r_{DH}^2 h_D}$ | $\frac{v_{iD}}{h_D}$ | $\frac{v_{iD}}{6.7 r_{ED}^2 h_E}$ | $\frac{v_{iD}}{2.6 h_E}$ | $\frac{v_{iE}}{h_E}$ |
| Sample 1 | 0.05 kHz                          | 2.5 kHz              | 1.3 kHz                           | 19 kHz                   | 280 kHz              |
| Sample 2 | 0.13 kHz                          | 2.5 kHz              | 0.8 kHz                           | 20 kHz                   | 490 kHz              |

Rayleigh wave with shorter wavelength decays more rapidly with depth, resulting in little penetration into, and hence influence of, the hypodermis.

Table 1 shows the formula to calculate the characteristic frequencies for skin. The distinct lower and higher characteristic frequency ranges corresponding to the D-H and E-D interfaces (respectively) justify our use of the dual bilayer model for skin, with the D-H bilayer used to model skin in the low frequency regime, and the E-D bilayer used in the high frequency regime. As a rule of thumb, an ideal low-frequency range should span from  $f_2$  of the D-H layer,  $f_2^{DH}$ , to the smaller of  $f_1$  of the D-H layer and  $f_2$  of the E-D layer; that is,  $f_2^{DH} < f < \min(f_1^{DH}, f_2^{ED})$ . Likewise, an ideal high-frequency range should span from the larger of  $f_1$  of the D-H layer and  $f_2$  of the E-D layer, to  $f_1$  of the E-D layer,  $f_1^{ED}$ . We find that  $f_1^{ED}$  is typically a few hundred kHz, a frequency too high to measure with OCE. For skin tissues, we find the measurement uncertainty increases greatly at frequencies higher than tens of kHz because of strong wave attenuation and interference with other waves such as supershear surface waves [34, 35]. This high-frequency range can be expressed as  $\max(f_1^{DH}, f_2^{ED}) < f < 0.5 f_{12}^{ED}$ . The factor 0.5 is

somewhat arbitrarily chosen (instead of 1) as it can give a sufficient range for reliable fitting. Table 1 shows the typical values of the characteristic frequencies for two skin-like samples. For sample 1,  $E_E=1500$  kPa,  $E_D=48$  kPa,  $E_H=6.8$  kPa,  $h_E=80$   $\mu\text{m}$ , and  $h_D=1$  mm, and for sample 2,  $E_E=4570$  kPa,  $E_D=52$  kPa,  $E_H=18$  kPa,  $h_E=80$   $\mu\text{m}$ , and  $h_D=1$  mm. The estimated low frequency range is approximately 0.1 to 1 kHz, and the high-frequency range is approximately 3 to 10 kHz. To further minimize the impact of hypodermis on E-D bilayer, we use the range of 4–10 kHz in the following study.

At frequencies between  $\min(f_1^{DH}, f_2^{ED})$  and  $\max(f_1^{DH}, f_2^{ED})$ , the Rayleigh wave speed is influenced by all three layers. Now we see that for the dual bilayer skin model to be valid, the following two conditions should be met:  $f_1^{DH} < 0.5 f_{12}^{ED}$  and  $f_2^{DH} < f_2^{ED}$ . The first condition requires  $\bar{h}_D > 5.2 h_E$ . And the second condition demands  $\frac{E_E E_H^2}{E_D^3} < (\frac{\bar{h}_D}{h_E})^2$ , which reduces to  $E_E E_H^2 / E_D^3 < 27$  using the first condition. These two geometrical and stiffness conditions are satisfied for skin tissues.

We can calculate the Young's moduli of all 3 layers using the following approach (Fig. 2):

- (1) Determine the Young's modulus of the hypodermis  $E_H$ . The bulk shear wave velocity of the hypodermis  $v_{iH}$  is equal to the measured wave velocity near  $f_2^{DH}$  (0.1–0.2 kHz).  $E_H = 3\rho v_{iH}^2$ , where  $\rho = 1$  g/cm<sup>3</sup>.
- (2) Determine the initial estimate of Young's modulus of the dermis  $E_{D(0)}$  by fitting the dispersion relation of the D-H bilayer,  $v = v(h_D, E_{D(0)}, E_H; f)$  in the low frequency range (0.2–1 kHz); and then determine the initial estimate of Young's modulus of the epidermis  $E_{E(0)}$  by fitting the dispersion of the E-D bilayer,  $v = v(h_E, E_{E(0)}, E_{D(0)}; f)$  in the high frequency range (4–10 kHz). The epidermal thickness  $h_E$  and dermal thickness  $h_D$  are determined from the OCT image. If the optical penetration depth of the OCT image is smaller

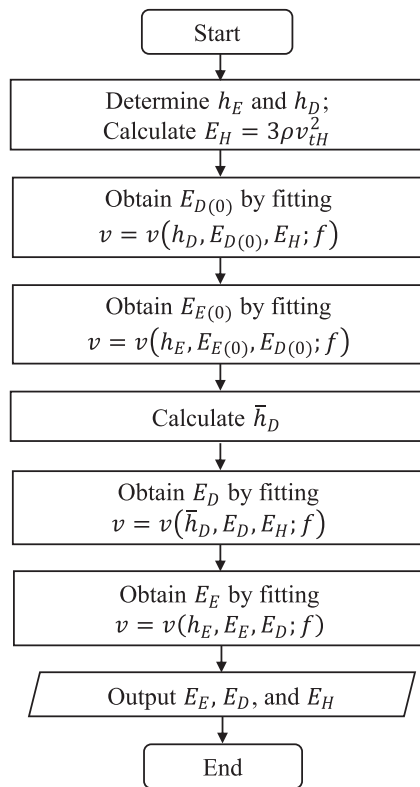


**Fig. 2.** Flowchart of the inverse approach to determine the Young's modulus of the three layers.

than  $h_D$ , then set  $h_D = 1$  mm.  $E_{D(0)}$  is an overestimation of  $E_D$ , and  $E_{E(0)}$  is an underestimation to  $E_E$  by  $\sim 10\%$ .

- (3) Calculate the equivalent thickness of the dermis  $\bar{h}_D = \bar{h}_D(h_D, h_E, \frac{E_{E(0)}}{E_{D(0)}})$  (Eq. (1) or Eq. (B.3) in Appendix B). ( $\bar{h}_D$  is not so sensitive to  $\frac{E_{E(0)}}{E_{D(0)}}$ . The bias in  $\bar{h}_D$  propagating from  $\frac{E_{E(0)}}{E_{D(0)}}$  is  $\sim 2\%$ .)
- (4) Determine  $E_D$  by fitting the dispersion relation of the D-H bilayer again,  $v = v(h_D, E_D, E_H; f)$  in the low frequency range (0.2–1 kHz), and then determine  $E_E$  by fitting the dispersion of the E-D bilayer again,  $v = v(h_E, E_E, E_D; f)$  in the high frequency range (4–10 kHz).
- (5) Output  $E_E, E_D,$  and  $E_H$ .

In step (2) and step (3), the curve fitting uses root-mean-square-error (RMSE) as an objective function. Best fitting is found by searching for the minimum error. Because there is only one variable in each fitting, the fitting complexity is greatly reduced compared to multi-parameter fitting used in inversion models.

### 2.3. Verification with numerical simulation

We used finite element analysis (FEA) to validate the theoretical dispersion relation of surface wave propagation in skin and our inverse approach (details on the FEA can be found in Supplementary Information S1). We built the FEA model using commercial software (Abaqus 6.12, Dassault Systèmes). The model contains three layers, each with different thickness and Young's modulus, to simulate the epidermis ( $h_E = 80 \mu\text{m}$ ,  $E_E = 1500$  kPa), dermis ( $h_D = 1$  mm,  $E_D = 48$  kPa), and hypodermis (semi-infinite,  $E_H = 6.75$  kPa). The density of each layer is assumed to be constant,  $\rho = 1$  g/cm<sup>3</sup>. Surface waves are excited by applying local oscillating pressure on the surface. Fig. 3(a) shows the simulated cross-

sectional displacement profiles of the surface waves at different frequencies. At 0.25 kHz, the wavelength of the surface wave is much greater than the combined thickness of the epidermis and dermis. At 4 kHz, the surface wave is leaky in the hypodermis and much of its elastic energy resides in the dermis. At 10 kHz, the surface wave is leaky in both dermis and hypodermis, and a considerable part of its elastic energy is present in the epidermis.

Fig. 3(b) shows the phase velocities (black circles) obtained by FEA at various frequencies in the range of 0.1 to 10 kHz. By performing the inverse analysis on the FEA data we obtain the Young's modulus for each layer. The Young's modulus of the hypodermis inferred from the phase velocity at 100 Hz is 8.7 kPa, which is  $\sim 28\%$  larger than the input value. This overestimation is due to  $f_2^{DH} \approx 50$  Hz  $< 100$  Hz (see Table 1), which can be eliminated if the phase velocity below 50 Hz is available. Such a bias in the Young's modulus of hypodermis has a negligible effect on subsequent analysis. We further estimate the Young's moduli for the dermis and epidermis as 47 kPa and 1530 kPa, which are in excellent agreement with the values we used in the numerical simulation (48 kPa ( $-2\%$ ) and 1500 kPa ( $+2\%$ )). The final fitting curves are shown in Fig. 3(b). The key frequencies,  $f_2^{DH}$ ,  $f_1^{DH}$ , and  $f_2^{ED}$ , described in the Section 2.2 and Table 1 are also indicated (red and blue circles).

## 3. Experimental validation using skin-mimicking 3-layer phantoms

### 3.1. OCE system

The OCE system has been described previously [27, 28]. In brief, the system uses a swept-source laser with a center wavelength of 1300 nm and a bandwidth of 108 nm at a sweep rate of 43 kHz. The axial resolution is  $\sim 15 \mu\text{m}$ . In the sample arm, the laser beam is scanned by a pair of galvanometer mirror scanners (Cambridge Technology, 6210H), and focused by a wide-aperture scan lens (Thorlabs, LSM54–1310) yielding a long working distance of 64 mm and a transverse resolution of  $\sim 30 \mu\text{m}$ . The illumination power on the skin is  $\sim 15$  mW, which complies with the ANSI-Z136.1–2014 safety standard. An input/output board (National Instruments, USB-6353) is used to generate analog waveforms for the galvanometer scanners and a piezoelectric actuator used to excite surface waves. The wavelength sweep cycle of the laser is used to synchronize data acquisition, beam scanning, and probe actuation, providing an absolute phase reference for the detection of surface waves.

Mechanical stimulation was achieved using a custom-made contact mechanical actuator. The tip of the actuator (Fig. 4a) is 3D-printed from a biocompatible polymer (Formlabs Surgical Guide Resin). It has the shape of a triangular prism, of which the rectangular face is glued to a piezoelectric transducer (PZT) (Thorlabs, PA4CEW), and a 2 mm-long edge contacts the sample. The particular shape of the contact actuator was chosen to excite an elastic wave with a linear wavefront. The linear wave has lower geometrical attenuation than circular waves that could be generated with a spherical tip. This orientation of the prism-like shape allowed us to measure the waves as closely to the contact region or the source as possible. This is critical for the measurement of the high frequency surface waves, which are attenuated rapidly with distance from the source due to viscoelasticity of the medium. The contact length of the tip on the skin is  $\sim 0.5$  mm, approximately a half wavelength of the mechanical wave at high frequencies. So, the excitation stress profile is well matched to the stress profile of the wave for efficient excitation of the wave. At low frequencies, the mode matching is less critical because the wave amplitudes are larger. We used this optimized tip to generate the mechanical waves for all frequencies. Pure tone stimuli were chosen with a frequency range of 0.1–10 kHz. The exact frequencies tested

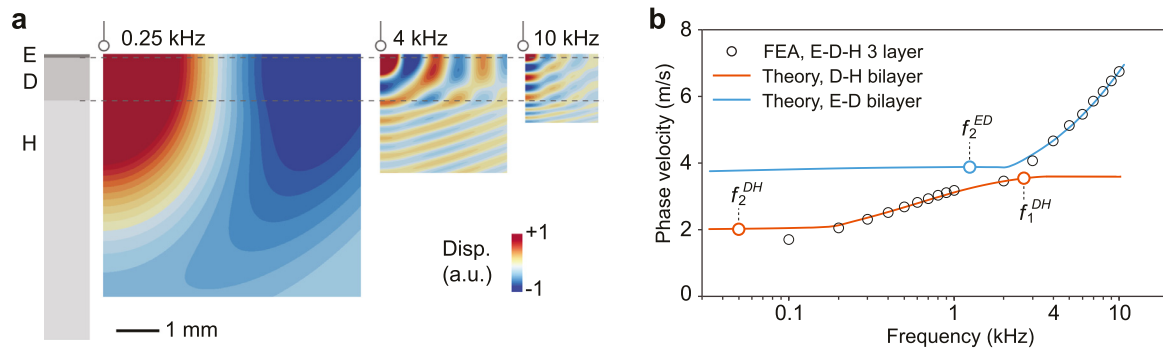


**Fig. 3.** Numerical simulation of surface waves in skin. (a) Finite element simulations showing the vertical displacement profiles of leaky Rayleigh surface waves in the 3-layer model at three representative frequencies: 0.25 kHz, 4 kHz, and 10 kHz. The location of the excitation sources for each plot are indicated at the top left by a circle-and-line). (b) Dispersion relation of the Rayleigh surface waves. Black circles, FEA simulation data. Red curve: Analytical theory obtained from the D-H bilayer model. Blue curve: Analytical theory obtained from the E-D bilayer model.

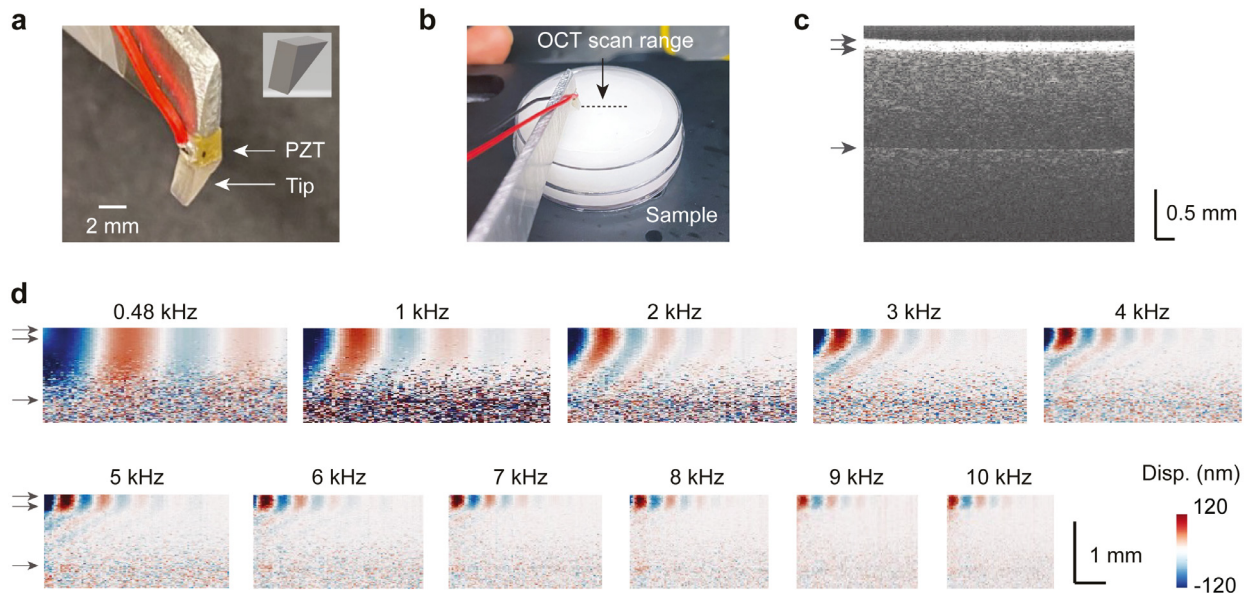


**Fig. 4.** Surface wave propagation in a three-layer skin-mimicking sample. (a) Picture of the contact actuator composed of a piezoelectric transducer (PZT) and a prism-shaped plastic tip. The inset is a three-dimensional drawing of the tip. (b) Picture of the 3-layer phantom. Dashed line, the OCT beam scan path. (c) OCT image of the phantom. Arrows indicate the demarcation lines between layers. (d) Displacement profiles of surface waves excited at different frequencies.

range from 120 Hz to 840 Hz with an interval of 120 Hz and then from 1 kHz to 10 kHz with an interval of 1 kHz. Above 10 kHz, the increasingly short wavelength and low displacement amplitude made OCE measurements unreliable.

The system is operated in M-B mode. At each transverse location,  $m$  consecutive A-lines were acquired. After completing an M-scan, the sample arm beam was moved to the next transverse location and the measurement was repeated. In total, 96 transverse positions were scanned. At each transverse location, the acquisition time was about 0.4 s with  $m = 172$  for each of the 10 stimulus frequencies between 1 and 10 kHz, and the acquisition time was 1 to 5 s with  $m = 400$  for each of the 7 stimulus frequencies between 120 and 840 Hz. In total, an M-scan at 17 frequencies took about 20 s. Since the propagation length decreases with increasing frequency, the sample arm scan length  $L$  was varied inverse-linearly with frequency:  $L$  [mm] =  $8.5 - 0.5 * f$  [kHz] at 1 to 10 kHz,  $L = 8$  mm for 0.24 to 1 kHz, and  $L = 14$  mm for 0.12 kHz.

The propagation of the Rayleigh surface wave was analyzed from the displacement measured at the surface using the method previously described [27, 28]. In summary, we extracted displacement profiles over time  $t$  at each transverse location, and then performed a 1-dimensional Fourier transform to move the data from time  $t$  domain to frequency  $f$  domain. Next, the frequency domain

data was filtered at the driving frequency to obtain lower noise waveforms. After we obtained the displacement profiles over the  $x$  coordinate, another 1-dimensional Fourier transform moved the data from the spatial  $x$  domain to the wavenumber  $k_x$  domain. The wavenumber  $k$  of the surface wave was then determined from the plot by selecting the peak corresponding to the Rayleigh surface wave. This filtering in the  $k_x$  domain is critical to remove other higher-order modes especially at high frequencies [35]. The phase velocity is then  $v = 2\pi f/k$ .

The single-pixel vibration sensitivity of the system was previously measured to be  $\sim 4$  nm when the optical SNR was 30 dB [36]. We typically obtain an optical SNR  $> 30$  dB at the surface of the phantom and skin. Since a single M-scan consists of  $m$  ( $= 172$ ) A-line data points, we expect the final amplitude sensitivity to be  $4/\sqrt{m} = 0.3$  nm. The wave amplitude decreases at higher frequencies, but we typically obtain  $> 20$  nm amplitude at 10 kHz for the skin (Supplementary Fig. 3) and a high wave-amplitude SNR of  $> 18$  dB.

### 3.2. Phantom validation results

To validate the method we prepared 3-layer skin-mimicking phantoms [15, 37]. First, a hypodermal layer was prepared using

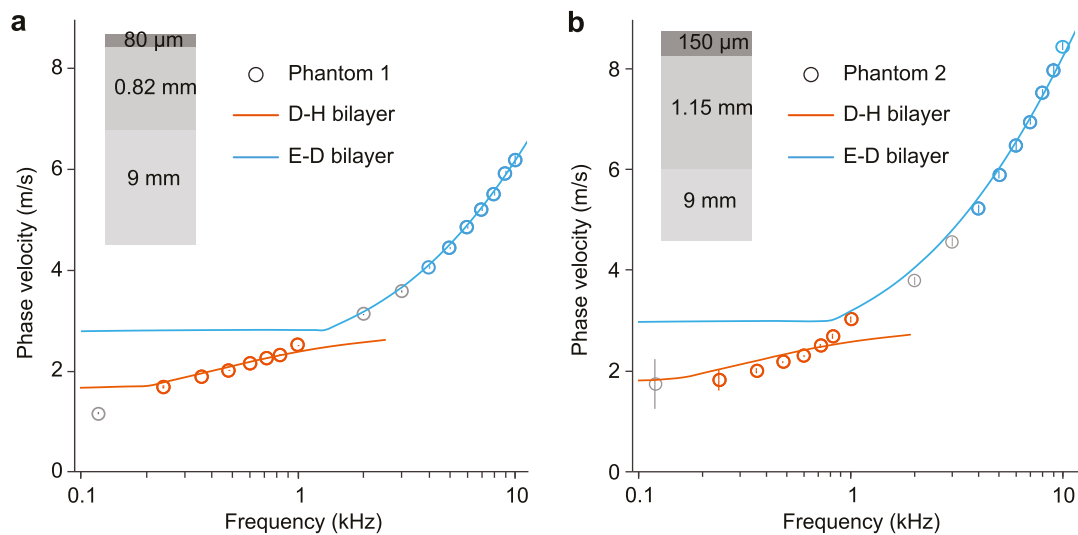


**Fig. 5.** Phase velocity dispersion curve and model fitting in (a) phantom #1, and (b) phantom #2. Dots and error bars, mean and standard deviation of three measurements at three different locations. Red line, D-H bilayer model with best fit in 0.24 to 1 kHz. Blue line, E-D bilayer model with best fit in 4 to 10 kHz.

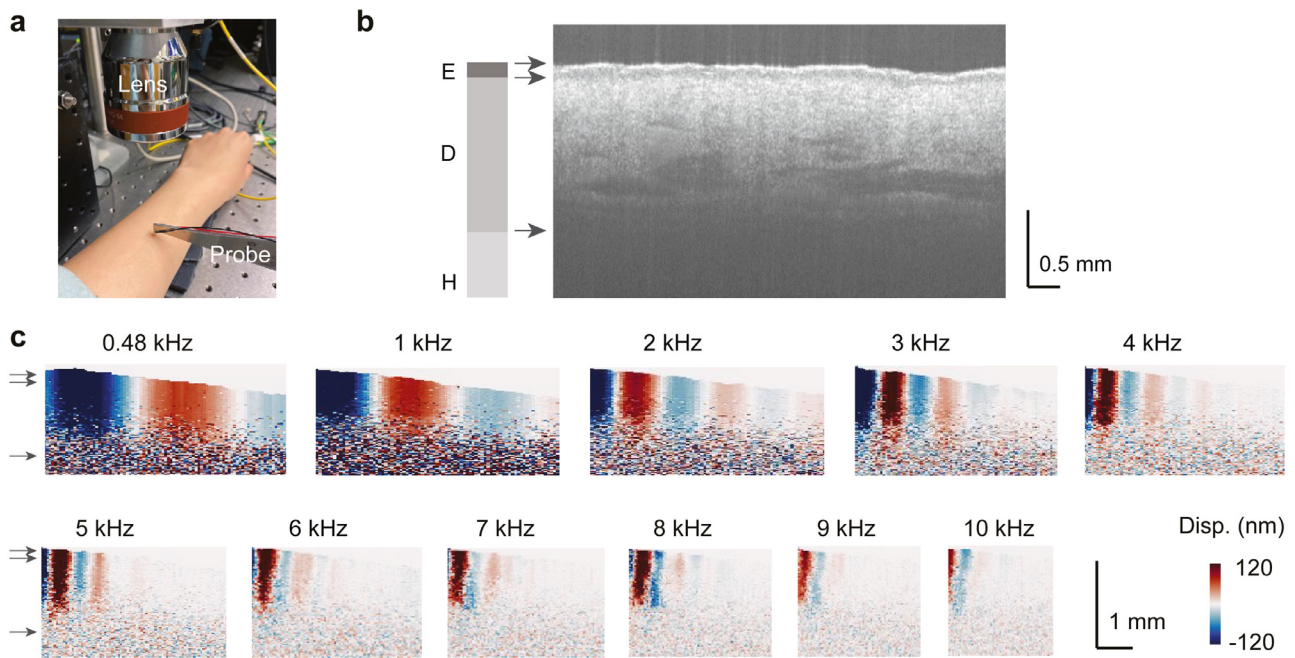


**Fig. 6.** Surface wave propagation in human skin in vivo. (a) Picture of a forearm during measurement. (b) OCT images of forearm (E: epidermis, D: dermis, H: hypodermis). Arrows indicate the demarcation lines between layers. (c) Displacement profiles of surface waves excited at different frequencies. The skin layers are labeled on the 0.48 kHz and 5 kHz images.

a hydrogel with 3% gelatin concentration on a 35-mm Petri dish. Then, a gelatin hydrogel layer of 7% concentration was deposited for the dermis. Finally, a thin polydimethylsiloxane (PDMS) layer for the epidermis was deposited using a standard 10:1 mixing ratio of base elastomer and curing agent (Sylgard 184, Dow Corning). Two different phantoms with slightly different layer thicknesses were investigated in this study, as shown in Table 2. The thicknesses of the first and second layers were measured using OCT assuming a mean refractive index of 1.4. The total thickness of each phantom was ~ 10 mm.

The measured reference material properties are shown in Table 2. Details for the measurement can be found in Supplementary S2. In brief, the Young’s moduli of the middle and bottom layers were measured from the measurement of Rayleigh surface wave speeds in bulk gelatin phantoms with 7% and 3% gelatin con-

centrations, respectively. The Young’s modulus of the top layer was measured from measuring the Lamb waves in a 150 μm PDMS film that we harvested from the top layer of the phantom #2 after the experiment. We estimated the Young’s modulus of the film hanging in the air by fitting the dispersion curve (1 to 10 kHz) with the Lamb wave model [28].

Fig. 4(b) shows the setup of the piezoelectric excitation source and sample. Fig. 4(c) shows a representative intensity image, in which the three layers are readily distinguished. The cross-sectional vibrography images reveal the vertical displacement profiles of the surface wave excited at different frequencies (Fig. 4(d)). As the frequency increases, the surface wavelength and propagation length, as well as the depth penetration of the surface wave decrease. Note that the full penetration depth of the surface waves at low frequencies such as 0.48 and 1 kHz is not visible on the

**Table 2**  
Specifications of the tissue phantoms and measured data.

|   |        | Phantom #1          | Phantom #2          |
|---|--------|---------------------|---------------------|
| Layer thickness                                     | Top    | 80 $\mu\text{m}$    | 150 $\mu\text{m}$   |
|   | Middle | 0.82 mm             | 1.15 mm             |
|   | Bottom | 9 mm                | 9 mm                |
| Young's modulus, reference (mean $\pm$ std.)        | Top    | 1.13 $\pm$ 0.08 MPa |                     |
|   | Middle | 27 $\pm$ 2 kPa      |                     |
|   | Bottom | 9 $\pm$ 1 kPa       |                     |
| Young's modulus, estimated by OCE (mean $\pm$ std.) | Top    | 1.14 $\pm$ 0.03 MPa | 1.12 $\pm$ 0.05 MPa |
|   | Middle | 23 $\pm$ 0 kPa      | 26 $\pm$ 2 kPa      |
|   | Bottom | 9 $\pm$ 0 kPa       | 10 $\pm$ 2 kPa      |

**Table 3**  
Young's moduli in the forearm skin tissues of two human subjects.

|  |            | Subject #1          | Subject #2          |
|--|------------|---------------------|---------------------|
| Layer thickness                            | Epidermis  | 80 $\mu\text{m}$    | 82 $\mu\text{m}$    |
|  | Dermis     | 1 mm                | 1 mm                |
|  | Hypodermis | –                   | –                   |
| Measured Young's modulus (mean $\pm$ std.) | Epidermis  | 4.57 $\pm$ 0.27 MPa | 3.48 $\pm$ 0.14 MPa |
|  | Dermis     | 52 $\pm$ 7 kPa      | 27 $\pm$ 1 kPa      |
|  | Hypodermis | 18 $\pm$ 2 kPa      | 12 $\pm$ 1 kPa      |

images because of insufficient optical SNR below a depth of approximately 1 mm. The displacement amplitude of the waves near the contact tip were between 50 and 200 nm (Supplementary Fig. S3).

Fig. 5 shows the phase velocity dispersion curves measured from the two phantoms and corresponding fitting results. The wave speed measured at the lowest frequency 0.12 kHz was often erroneous because the wavelength of the wave ( $\sim 20$  mm) is greater than the thickness of the sample (10 mm), so the wave speed measurement is influenced by the spurious waves reflected from the bottom interface between the 3% gel and the plastic dish. Therefore, the phase velocity measured at 0.24 kHz was used for estimating the Young's modulus of the bottom 3% gel layer. Supplementary Fig. S4 shows the plots of dimensionless root-mean-square-error (RMSE) with the fitting parameter of wave phase velocity. For the fitting shown in Fig. 5(a), the dimensionless RMSE values for the D-H bilayer and the E-D bilayer are 0.029 and 0.002, and the  $R^2$  values are 0.978 and 0.999, respectively. In Fig. 5(b), the dimensionless RMSE values for the D-H bilayer and the E-D bilayer are 0.074 and 0.006, and the  $R^2$  values are 0.885 and 0.999, respectively. Table 2 shows that the estimated Young's modulus matches well with the reference values.

#### 4. Results on human skin in vivo

We performed in vivo measurements of the dorsal forearm skin of two healthy volunteers (Subject #1: male; Subject #2: female, both in early 30 s of age). The study was conducted at the Massachusetts General Hospital (MGH) following approval from the Institutional Review Board (IRB) of Massachusetts General Hospital and the Mass General Brigham Human Research Office. Written informed consent was obtained from both subjects prior to the measurement and all measurements were performed in accordance with the principles of the Declaration of Helsinki. Hairs in the measurement area in the forearm were gently removed using an eyebrow razor. Fig. 6 presents the measurement results from Subject #1. The epidermis/dermis interface was segmented using a custom algorithm by analyzing light intensity in the OCT image (Fig. 6(b)). The thickness of the epidermis was calculated as the average optical thickness between the two interfaces divided by an assumed refractive index of 1.4. The dermis/hypodermis interface was not clearly identified due to the limited optical penetration depth of the OCT system. The typical dermal thickness of healthy

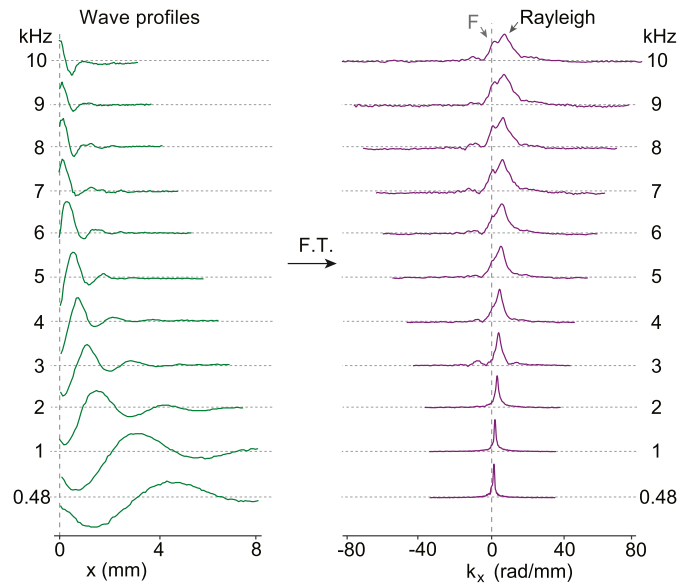


**Fig. 7.** Extracting wave speeds from skin. Left: displacement waveforms as a function of the propagation distance. Right: the corresponding spatial frequency representation obtained by the Fourier Transform. In the spectra at higher frequencies ( $> 4$  kHz), the primary peak with a higher wave number comes from the Rayleigh surface wave, whereas the secondary peak with a lower wave number is due to fast (F) supershear elastic wave [34, 35].

forearm skin has been reported to be  $1.08 \pm 0.16$  mm (mean  $\pm$  std.) [2]; therefore, the thickness of the dermis was assumed to be 1 mm for both subjects. Fig. 6(c) shows the cross-sectional displacement profiles at different frequencies. The wave displacement amplitudes measured near the tip were  $\sim 200$  nm up to 1 kHz and decreased to 20–30 nm at 10 kHz (Supplementary Fig. S3).

Fig. 7 shows the displacement waveforms and the corresponding wavenumber domain plots at different frequencies. Besides the clearly defined Rayleigh wave peak, the secondary peak corresponding to a higher-order fast elastic wave appearing at high frequencies  $> 4$  kHz. This fast wave were identified as the supershear surface wave [34, 35], which is excited more efficiently by the piezoelectric actuator as its wavelength becomes  $< 20$  mm. The

**Table 4**  
Young's modulus values estimated from different dermal thicknesses. Values in [ ] are % differences compared to Table 3.

| Subject #  | Dermal thickness | 0.9 mm [-10%]    | 1.1 mm [+10%]  | 1.25 mm [+25%] |
|------------|------------------|------------------|----------------|----------------|
| Subject #1 | Epidermis        | 4.40 MPa [-4%]   | 4.69 MPa [+3%] | 4.80 MPa [+5%] |
|            | Dermis           | 55 kPa [+8%]     | 48 kPa [-6%]   | 45 kPa [-12%]  |
| Subject #2 | Epidermis        | 3.53 MPa [-0.3%] | 3.62 MPa [+2%] | 3.66 MPa [+3%] |
|            | Dermis           | 29 kPa [+4%]     | 26 kPa [7%]    | 25 kPa [-11%]  |

**Table C1**  
Young's modulus of in vivo forearm skin in the literature .

| Reference     | # Subjects | Young's modulus (kPa)                                      | Method                             | Frequency    |
|---------------|------------|--|------------------------------------|--------------|
| Li [13]       | 12         | 60 – 88 (dermis) 6 – 14 (hypodermis)                       | Shear wave elastography            | ~ 1 kHz      |
| Zhou [17]     | 11         | 214 ± 106 (epidermis) 49 ± 26 (dermis) 10 ± 4 (hypodermis) | Surface acoustic wave elastography | < 4 kHz      |
| Li [39]       | 1          | ~ 500 (epidermis)  | Compression OCE                    | Quasi-static |
|               |            | ~ 150 (dermis) ~ 50 (hypodermis)                           | Surface acoustic wave elastography | < 4 kHz      |
| Li [14]       | 5          | 150 – 286 (dermis) 49 – 58 (hypodermis)                    | Surface acoustic wave elastography | < 4 kHz      |
| Chartier [11] | 1          | ~ 142 (dermis) ~ 20 (hypodermis)                           | Transient elastography             | 100 – 500 Hz |
| Liu [18]      | 8          | 10 ± 4 (bulk)  | Air-puff OCE                       | ~400 Hz      |
| Liang [15]    | 1          | 69 ± 25 (bulk)   | Dynamic OCE                        | 50 Hz        |
| Zhang [56]    | 30         | 14 ± 10 (bulk)   | Surface acoustic wave elastography | 100 – 400 Hz |
| Boyer [57]    | 46         | 5 – 13 (bulk)  | Dynamic indentation                | 10 Hz        |
| Hendriks [58] | 10         | ~ 56 (bulk)  | Suction test                       | Quasi-static |
| Sanders [59]  | 19         | 23 – 107 (bulk)  | Torsion test                       | Quasi-static |

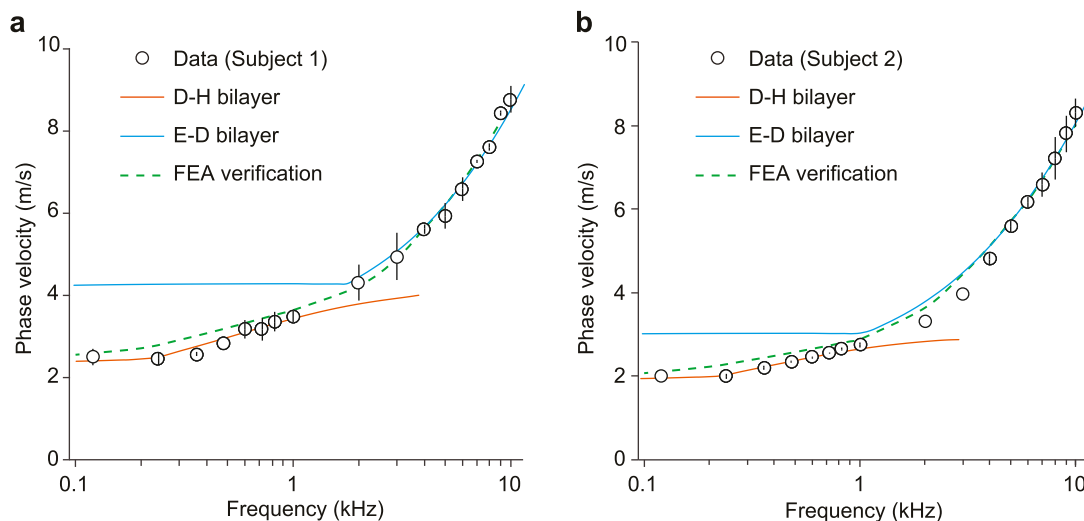


**Fig. 8.** Phase velocity dispersion curve and model fitting for (a) Subject #1, and (b) Subject #2. Dots and error bars, mean and standard deviation of three measurements at approximately the same location. Red line, D-H bilayer model with best fit in 0.24–1 kHz. Blue line, E-D bilayer model with best fit in 4–10 kHz. Green dashed line, FEA verification using the parameters determined by the dual-bilayer algorithm.

Rayleigh wave velocity was determined from the primary peak in the wavenumber profiles.

Fig. 8 compares the measured phase velocity dispersion curves of the two human subjects and the corresponding fitting results. Each data point and its error bars correspond to the mean and standard deviation of three OCE scans that were performed at the same location. Between measurements, the excitation actuator was displaced from the skin and then brought back to approximately the same location on the tissue with the same gentle contact pressure. The repeatability of the measurement was limited by subject motion. The wave velocities measured at 0.12 kHz were slightly higher than those at 0.24 kHz. This could possibly be explained by the interference of spurious waves reflected from the boundaries, such as the muscle and bone underneath the hypodermis. For both subjects, fitting results demonstrate clear transitions of the experimental data from the D-H bilayer in the low frequency regime to the E-D bilayer in the high frequency regime. For Fig. 8(a), the dimensionless RMSE values for the D-H bilayer and the E-D bilayer are 0.024 and 0.004, and the  $R^2$  values are 0.960 and 0.987, respectively. For Fig. 8(b), the dimensionless RMSE values for the D-H bi-

layer and the E-D bilayer are 0.018 and 0.005, and the  $R^2$  values are 0.994 and 0.997, respectively.

Table 3 displays the measured Young's modulus for the two subjects. The elasticity values vary distinctly between the two subjects in all three layers. To validate our inverse approach, we performed additional finite element analyses with the parameters in Table 3 and plotted the theoretical dispersion relations of the Rayleigh surface waves. The simulations show good agreements with the experiments (Fig. 8 and Supplementary Fig. S5).

### 5. Discussion and conclusion

Using an advanced OCE system optimized for efficient excitation and detection of surface waves, we have measured wave phase velocities in human skin in vivo over a wide frequency range up to 10 kHz, allowing us to estimate the Young's modulus of different tissue layers. We have shown that high frequency measurement is essential to resolve the thin epidermis, while low frequency measurement permits access to the deep hypodermis. Previous studies have been restricted to frequencies < 4 kHz because of limited

sensitivity to the reduced displacement amplitude at higher frequencies. For the same wave energy, the displacement amplitude of an elastic wave decreases as the square of the frequency. That is, the displacement amplitude at 10 kHz would be  $\sim 6.3$  times smaller than the amplitude at 4 kHz. To overcome this challenge, our OCE system uses appropriate M-mode averaging to enhance sensitivity without adding motion artifacts. We also optimized the shape and dimensions of the actuator tip to maximize the excitation efficiency at high frequencies. For efficient generation of high frequency waves, the excitation stress profile must be well matched to the stress profile of the wave at high frequencies. This condition is achieved when the contact length is approximately a half wavelength of the mechanical wave. These advances enabled us to make OCE measurements of the skin at frequencies up to 10 kHz.

It is interesting to compare our results with previously reported values of *in vivo* skin stiffness in the literature (see Appendix C Table C1). Our measured Young's moduli of the dermis and hypodermis are in reasonable agreement with previous results obtained at lower frequencies. However, our values for the epidermis ( $\sim 3.5$  MPa) are significantly higher than those obtained using lower frequency measurements. In particular, the previous OCE measurement in a 0.2–4 kHz range [17] estimated the epidermis stiffness to be  $\sim 200$  kPa. We suspect that this rather low value is due to the limited frequency causing some averaging of epidermis and dermis, resulting in underestimation of the epidermis stiffness. Because of the viscoelasticity of skin tissues, the Young's modulus is expected to be significantly higher at 1 kHz than at 1 Hz [38]. Hence, our stiffness values are expected to be higher compared to quasi-static stiffness values. Indeed, compression-based OCE [39] measures Young's modulus at  $< 1$  Hz. We also compare our results with previous mechanical test results of excised skin tissues. The reported Young's moduli obtained by quasi-static tensile test showed large variations ranging from 5 kPa [3] to 11 MPa [40], highly subject to the load rate, levels of stress and strain applied to the skin, and the method to evaluate Young's modulus [41]. In other studies using quasi-static indentation test, the Young's modulus of the epidermis sheet was measured to be 1–2 MPa [42]. Our measured values of 4 MPa in the epidermis are within the previous range. The Young's modulus of subcutaneous fat was previously measured to be 3.2 kPa using quasi-static indentation [43]. This value is smaller than our values of 12–18 kPa at 0.24 kHz because of the viscoelastic properties of the skin. Besides, the dynamic Young's moduli at kHz frequencies are thought to be higher than quasi-static Young's moduli (see discussion below).

Our results showed that the epidermis is about 100 times stiffer than the dermis. This is because of the contribution of the stiff stratum corneum (SC). A normal, dry SC has a considerably higher stiffness, between 100 MPa and 1 GPa [44]. Across most of the body, including the forearm, the thickness of the SC is  $\sim 20$   $\mu\text{m}$  [45], which is too thin to be resolved by OCE at frequencies up to 10 kHz. Therefore, our measured stiffness is an average of the SC and the viable epidermis. In contrast, skins at the palm and fingertip have a SC thickness as large as 200  $\mu\text{m}$  [2, 45]. The algorithm and guideline described here should be applicable to all types of skin tissues in the various sites of the human body. For relatively stiff tissues, such as skins in a low hydration state, it may be necessary to extend the measurement frequency range beyond 10 kHz to satisfy the high-frequency condition.

Our current model assumes that the layers making up skin tissue are elastic, linear, and isotropic. To evaluate the impact of dermal viscosity on the epidermis-dermis bilayer, we assume the dermal viscoelasticity follows the power law model  $\nu \propto f^m$  with  $m = 0.4$ , a representative value for soft tissues [46]. In this case, the shear wave speed in the dermis will increase with  $f$ . After con-

sidering the dermal viscoelasticity, we refit the epidermis-dermis bilayer model into the 4 – 10 kHz data of subject #1. The new fitting result shows that the Young's modulus of the epidermis is  $\sim 3.9$  MPa, which is 15% smaller than the original fitting result of  $\sim 4.57$  MPa (Supplementary Fig. 6). Therefore, an overestimation in the epidermis stiffness (by  $\sim 15\%$ ) can result from ignoring the viscoelastic dispersion of the dermis. Future work should improve the dual bilayer model by considering the representative viscosity values of skin layers [47, 48].

Due to the limited imaging depth of our OCT system, the thickness of the dermis might have been underestimated. The overestimation of the dermal thickness results in overestimating the stiffness of the epidermis and underestimating the stiffness of the dermis. Table 4 shows the estimated Young's moduli obtained from using different dermal thickness values reported in literature [2].

Our three-layer model is robust in evaluating the layered stiffness of skin. The lateral resolution of the method is currently limited by the wavelength of the wave at low frequencies ( $\sim 10$  mm). One promising direction that can overcome this limitation is to use the full-field displacement measured by OCE and perform wave inversion to get two-dimensional stiffness map. Such a full wave-form inversion for pure elastic conditions has been developed in the field of geophysics [49]. However, the viscoelastic nature of the skin may pose a challenge for such full-field OCE.

The variation of the skin thickness across the scan area is a potential source of error. The low frequency analysis is not sensitive to the thicknesses of the dermis and epidermis, but the high frequency analysis of the dermis and epidermis is sensitive to their thicknesses. However, for typical skin tissues their thickness tend not to vary significantly across the mm-scale span of the high-frequency waves.

While we have excluded the fast, supershear waves ('F' waves in Fig. 7) in this study, the leaky surface waves can provide additional mechanical information about the skin. Recently we discovered that these waves are highly sensitive to the mechanical anisotropy and local stress [35]. The in-plane strain of forearm skin is less than 5% [50]. At this low strain level, the influence of prestress on Young's modulus is deemed small [51]. We plan to use the supershear surface waves to characterize the stress field in the skin in a future study.

The broadband surface-wave OCE technique introduced here are expected to have several applications. For instance, it may prove useful for evaluating the influence of age, gender, and body site on the mechanical properties of the skin and for studying the impact of skin hydration and dryness [52], which is of great interest in the cosmetics industry. In addition, it may be useful in diagnosing skin diseases related to dryness and monitoring the therapeutic responses, such as xeroderma [53], atopic dermatitis [54], and ichthyosis [55]. Finally, besides dermatologic applications, this technique may be extended to characterizing other layered tissues, such as blood vessel walls, and other soft materials with a depth-dependent stiffness gradient.

#### Declaration of Competing Interest

None.

#### Supplementary materials

Supplementary material associated with this article can be found, in the online version, at doi:[10.1016/j.actbio.2022.04.030](https://doi.org/10.1016/j.actbio.2022.04.030).

#### Appendix

##### A. Surface waves in a semi-infinite bilayer structure

We consider surface waves within the  $x-z$  plane, propagating along the  $x$  axis. We introduce two potential functions  $\varphi_1$  and  $\varphi_2$ ,

and two stream functions  $\psi_1$  and  $\psi_2$  to decouple the transverse (shear) and longitudinal waves, which relate to the displacements of the film and the substrate by

$$u_x^f = \frac{\partial \varphi_1}{\partial x} + \frac{\partial \psi_1}{\partial z}, u_z^f = \frac{\partial \varphi_1}{\partial z} - \frac{\partial \psi_1}{\partial x}, u_x^s = \frac{\partial \varphi_2}{\partial x} + \frac{\partial \psi_2}{\partial z}, u_z^s = \frac{\partial \varphi_2}{\partial z} - \frac{\partial \psi_2}{\partial x} \tag{A.1}$$

where  $\mathbf{u}^f$  and  $\mathbf{u}^s$  denote the displacements in the film and the substrate, respectively. Then the equilibrium equations expressed in the forms of the potential and stream functions are

$$\frac{\partial^2 \varphi_i}{\partial x^2} + \frac{\partial^2 \varphi_i}{\partial z^2} = \frac{1}{v_{li}^2} \frac{\partial^2 \varphi_i}{\partial t^2}, \frac{\partial^2 \psi_i}{\partial x^2} + \frac{\partial^2 \psi_i}{\partial z^2} = \frac{1}{v_{ti}^2} \frac{\partial^2 \psi_i}{\partial t^2} \tag{A.2}$$

where  $v_{li} = \sqrt{(\lambda_i + 2\mu_i)/\rho_i}$ , and  $v_{ti} = \sqrt{\mu_i/\rho_i}$  are the speeds of the longitudinal and transverse waves ( $i = 1, 2$ ).  $\lambda_1, \mu_1$  and  $\lambda_2, \mu_2$  are the Lamé constants of the film and the substrate, respectively.  $\rho_i$  is the density.  $t$  is the time. Notice  $\mu_1$  and  $\mu_2$  are related to the Young's modulus of the top layer  $E_1$  and the substrate  $E_2$  by

$$\mu_1 = \frac{E_1}{2(1 + \nu_1)}, \mu_2 = \frac{E_2}{2(1 + \nu_2)} \tag{A.3}$$

where the Poisson's ratios  $\nu_1$  and  $\nu_2$  are close to 0.5 for soft tissues. Consider the plane waves propagating along the  $x$  axis, i.e.,  $\varphi_i = \varphi_{0i}(z) \exp[j(kx - \omega t)]$  and  $\psi_i = \psi_{0i}(z) \exp[j(kx - \omega t)]$  ( $i = 1, 2$ ), where  $\omega$  and  $k$  denote the angular frequency and wavenumber. Frequency is  $f = \omega/(2\pi)$ . Phase velocity is  $v = \omega/k$ .  $j = \sqrt{-1}$ .  $\varphi_{0i}$  and  $\psi_{0i}$  denote the wave amplitudes, of which the explicit expressions can be obtained by solving Eq. (2)

$$\begin{aligned} \varphi_{01} &= a_1 e^{-i\alpha_1 z} + b_1 e^{i\alpha_1 z}, \psi_{01} = c_1 e^{-i\beta_1 z} + d_1 e^{i\beta_1 z}, \\ \varphi_{02} &= a_2 e^{-i\alpha_2 z} + b_2 e^{i\alpha_2 z}, \psi_{02} = c_2 e^{-i\beta_2 z} + d_2 e^{i\beta_2 z} \end{aligned} \tag{A.4}$$

where  $\alpha_i = \sqrt{(\omega/v_{li})^2 - k^2}$ ,  $\beta_1 = \sqrt{(\omega/v_{t1})^2 - k^2}$ , and  $\beta_2 = \sqrt{(\omega/v)^2 - k^2}$ .  $b_2 = 0$  and  $d_2 = 0$  for the semi-infinite configuration. At the interface of the two layers, the displacements and stresses must be continuous, which yields

$$u_x^f = u_x^s, u_z^f = u_z^s, \sigma_{zz}^f = \sigma_{zz}^s, \sigma_{xz}^f = \sigma_{xz}^s, \tag{A.5}$$

and at the free surface, the following stress-free boundary conditions apply

$$\sigma_{zz}^f = 0, \sigma_{xz}^f = 0. \tag{A.6}$$

The Cauchy stresses  $\sigma_{xz}^i$  and  $\sigma_{zz}^i$  ( $i = 1, 2$ ) are determined via Hooke's law:

$$\sigma_{zz}^i = (\lambda + 2\mu) \frac{\partial u_z^i}{\partial z} + \lambda \frac{\partial u_x^i}{\partial x}, \sigma_{xz}^i = 2\mu \left( \frac{\partial u_x^i}{\partial z} + \frac{\partial u_z^i}{\partial x} \right). \tag{A.7}$$

Taking Eqs. (A.1), (A.4 – A.7), we get the following linear equation

$$\mathbf{M}_{6 \times 6} [a_1, b_1, c_1, d_1, a_2, c_2]^T = 0, \tag{A.8}$$

where

$$\mathbf{M} = \begin{bmatrix} k & k & -\beta_1 & \beta_1 & -k & \beta_2 \\ -\alpha_1 & \alpha_1 & -k & -k & \alpha_2 & k \\ \mu_1(k^2 - \beta_1^2) & \mu_1(k^2 - \beta_1^2) & -2\mu_1 k \beta_1 & 2\mu_1 k \beta_1 & -\mu_2(k^2 - \beta_2^2) & 2\mu_2 k \beta_2 \\ 2\mu_1 k \alpha_1 & -2\mu_1 k \alpha_1 & \mu_1(k^2 - \beta_1^2) & \mu_1(k^2 - \beta_1^2) & -2\mu_2 k \alpha_2 & -\mu_2(k^2 - \beta_2^2) \\ \mu_1(k^2 - \beta_1^2)e^{-i\alpha_1 h} & \mu_1(k^2 - \beta_1^2)e^{i\alpha_1 h} & -2\mu_1 k \beta_1 e^{-i\beta_1 h} & 2\mu_1 k \beta_1 e^{i\beta_1 h} & 0 & 0 \\ 2k\alpha_1 e^{-i\alpha_1 h} & -2k\alpha_1 e^{i\alpha_1 h} & (k^2 - \beta_1^2)e^{-i\beta_1 h} & (k^2 - \beta_1^2)e^{i\beta_1 h} & 0 & 0 \end{bmatrix}. \tag{A.9}$$

The existence of non-trivial solutions to Eq. (7) requires that the

determinant of  $\mathbf{M}$  is zero,

$$\det(\mathbf{M}) = 0, \tag{A.10}$$

From this equation, the dispersion relation of the surface waves is obtained.

### B. Equivalent thickness

To obtain an equivalent thickness  $\bar{h}_D$  for the dermis in the D-H bilayer, we take the long wavelength approximation. The bending stiffness of the E-D bilayer, denoted by  $K$ , is

$$K = \frac{1}{3} (E_D h_D^3 + E_E h_{DE}^3 - E_E h_D^3) - \frac{1}{4} \frac{(E_D h_D^2 + E_E h_{DE}^2 - E_E h_D^2)^2}{E_D h_D + E_E h_{DE} - E_E h_D}, \tag{B.1}$$

where  $h_{DE} = h_D + h_E$ .  $K$  governs the flexural deformation, playing a dominant role in determining the surface wave speed. The bending stiffness of the equivalent dermis layer is  $\frac{1}{12} E_D \bar{h}_D^3$ , which should be equal to  $K$ . Therefore, we obtain the equivalent thickness

$$\bar{h}_D = \left( \frac{12K}{E_D} \right)^{1/3}. \tag{B.2}$$

It can be written as

$$\bar{h}_D = h_D \left( \frac{4(E_D + E_E(1 + h_E/h_D)^3 - E_E)}{E_D} - \frac{3(E_D + E_E(1 + h_E/h_D)^2 - E_E)^2}{E_D(E_D + E_E(1 + h_E/h_D) - E_E)} \right)^{1/3}. \tag{B.3}$$

For  $E_D = E_E$ , we find  $K = \frac{1}{12} E_D h_{DE}^3$  and  $\bar{h}_D = h_D + h_E$ .

For thin epidermis, a Taylor expansion up to the second order of  $h_E/h_D$  gives

$$\bar{h}_D \approx h_D \left( \frac{1 + 4 \frac{E_E h_E}{E_D h_D} + 6 \frac{E_E h_E^2}{E_D h_D^2}}{1 + \frac{E_E h_E}{E_D h_D}} \right)^{1/3}. \tag{B.4}$$

For samples with very thin epidermis  $h_E \ll h_D$  and  $E_E h_E \gg E_D h_D$ , we find  $\bar{h}_D \approx 4^{1/3} h_D \approx 1.59 h_D$ . For thicker epidermis, yet thinner than dermis ( $h_E < h_D$ ), we obtain  $\bar{h}_D \approx 1.7 h_D$ .

### C. Previously reported stiffness values of human forearm skin in the literature

**Funding.** National Institutes of Health (NIH) (R01-EY025454, P41-EB015903).

**Disclosures.** The authors declare that there are no conflicts of interest related to this article.

**Supplemental document.** See **Supplement 1** for supporting content.

## References

- [1] J. Sandby-Moller, T. Poulsen, H.C. Wulf, Epidermal thickness at different body sites: relationship to age, gender, pigmentation, blood content, skin type and smoking habits, *Acta Dermato Venereologica* 83 (6) (2003) 410–413.
- [2] Y. Lee, K. Hwang, Skin thickness of Korean adults, *Surg. Radiol. Anat.* 24 (3–4) (2002) 183–189.
- [3] C.H. Daly, Biomechanical properties of dermis, *J. Invest. Dermatol.* 79 (1) (1982) 17–20.
- [4] C. Escoffier, J. de Rigal, A. Rochefort, R. Vasselet, J.-L. Léveque, P.G. Agache, Age-related mechanical properties of human skin: an in vivo study, *J. Invest. Dermatol.* 93 (3) (1989) 353–357.
- [5] J. Clark, J. Cheng, K. Leung, Mechanical properties of normal skin and hypertrophic scars, *Burns* 22 (6) (1996) 443–446.
- [6] S. Es'haghian, K.M. Kennedy, P. Gong, D.D. Sampson, R.A. McLaughlin, B.F. Kennedy, Optical palpation in vivo: imaging human skin lesions using mechanical contrast, *J. Biomed. Opt.* 20 (1) (2015) 016013.
- [7] A. Balbir-Gurman, C. Denton, B. Nichols, C. Knight, A. Nahir, G. Martin, C. Black, Non-invasive measurement of biomechanical skin properties in systemic sclerosis, *Ann. Rheum. Dis.* 61 (3) (2002) 237–241.
- [8] P. Agache, P. Humbert, *Measuring the Skin*, Springer Science & Business Media 2004.
- [9] A. Kalra, A. Lowe, A. Al-Jumaily, Mechanical behaviour of skin: a review, *J. Mater. Sci. Eng* 5 (4) (2016) 1000254.
- [10] J.-L. Gennisson, T. Baldeveck, M. Tanter, S. Catheline, M. Fink, L. Sandrin, C. Cornillon, B. Querleux, Assessment of elastic parameters of human skin using dynamic elastography, *IEEE Trans. Ultrason. Ferroelectr. Freq. Control* 51 (8) (2004) 980–989.
- [11] C. Chartier, Y. Mofid, C. Bastard, V. Miette, A. Maruani, L. Machet, F. Ossant, High-resolution elastography for thin-layer mechanical characterization: toward skin investigation, *Ultrasound Med. Biol.* 43 (3) (2017) 670–681.
- [12] C.C. Luo, L.X. Qian, G.Y. Li, Y. Jiang, S. Liang, Y. Cao, Determining the in vivo elastic properties of dermis layer of human skin using the supersonic shear imaging technique and inverse analysis, *Med. Phys.* 42 (7) (2015) 4106–4115.
- [13] G.-Y. Li, Y. Zheng, Y.-X. Jiang, Z. Zhang, Y. Cao, Guided wave elastography of layered soft tissues, *Acta Biomater.* 84 (2019) 293–304.
- [14] C. Li, G. Guan, R. Reif, Z. Huang, R.K. Wang, Determining elastic properties of skin by measuring surface waves from an impulse mechanical stimulus using phase-sensitive optical coherence tomography, *J. R. Soc., Interface* 9 (70) (2012) 831–841.
- [15] X. Liang, S.A. Boppart, Biomechanical properties of in vivo human skin from dynamic optical coherence elastography, *IEEE Trans. Biomed. Eng.* 57 (4) (2009) 953–959.
- [16] M. Kirby, P. Tang, H.-C. Liou, M. Kuriakose, J.J. Pitre, T.N. Pham, R. Ettinger, R. Wang, M. O'Donnell, I. Pelivanov, Probing Elastic Anisotropy of Human Skin in Vivo With Light Using Non-Contact Acoustic Micro-Tapping OCE and Polarization-Sensitive OCT, *Sci. Rep.* 12 (1) (2022) 1–17.
- [17] K. Zhou, K. Feng, C. Li, Z. Huang, A Weighted Average Phase Velocity Inversion Model for Depth-Resolved Elasticity Evaluation in Human Skin In-Vivo, *IEEE Trans. Biomed. Eng.* 68 (6) (2020) 1969–1977.
- [18] C.H. Liu, S. Assassi, S. Theodore, C. Smith, A. Schill, M. Singh, S. Aglyamov, C. Mohan, K.V. Larin, Translational optical coherence elastography for assessment of systemic sclerosis, *J. Biophotonics* 12 (12) (2019) e201900236.
- [19] S. Es'haghian, K.M. Kennedy, P. Gong, Q. Li, L. Chin, P. Wijesinghe, D.D. Sampson, R.A. McLaughlin, B.F. Kennedy, In vivo volumetric quantitative micro-elastography of human skin, *Biomed. Opt. Express* 8 (5) (2017) 2458–2471.
- [20] K.V. Larin, D.D. Sampson, Optical coherence elastography–OCT at work in tissue biomechanics, *Biomed. Opt. Express* 8 (2) (2017) 1172–1202.
- [21] M.A. Kirby, K. Zhou, J.J. Pitre, L. Gao, D.S. Li, I.M. Pelivanov, S. Song, C. Li, Z. Huang, T.T. Shen, Spatial resolution in dynamic optical coherence elastography, *J. Biomed. Opt.* 24 (9) (2019) 096006.
- [22] F. Zvietcovich, K.V. Larin, Wave-based optical coherence elastography: the 10-year perspective, *Prog. Biomed. Eng.* 4 (1) (2022) 012007.
- [23] J. Zhu, J. Yu, Y. Qu, Y. He, Y. Li, Q. Yang, T. Huo, X. He, Z. Chen, Coaxial excitation longitudinal shear wave measurement for quantitative elasticity assessment using phase-resolved optical coherence elastography, *Opt. Lett.* 43 (10) (2018) 2388–2391.
- [24] F. Zvietcovich, R.G. Gary, H. Mestre, M. Giannetto, M. Nedergaard, J.P. Rolland, K.J. Parker, Longitudinal shear waves for elastic characterization of tissues in optical coherence elastography, *Biomed. Opt. Express* 10 (7) (2019) 3699–3718.
- [25] F. Zvietcovich, P. Pongchalee, P. Meemon, J.P. Rolland, K.J. Parker, Reverberant 3D optical coherence elastography maps the elasticity of individual corneal layers, *Nat. Commun.* 10 (1) (2019) 1–13.
- [26] C. Li, G. Guan, X. Cheng, Z. Huang, R.K. Wang, Quantitative elastography provided by surface acoustic waves measured by phase-sensitive optical coherence tomography, *Opt. Lett.* 37 (4) (2012) 722–724.
- [27] A. Ramier, A.M. Eltony, Y. Chen, F. Clouser, J.S. Birkenfeld, A. Watts, S.-H. Yun, In vivo measurement of shear modulus of the human cornea using optical coherence elastography, *Sci. Rep.* 10 (1) (2020) 1–10.
- [28] A. Ramier, B. Tavakol, S.-H. Yun, Measuring mechanical wave speed, dispersion, and viscoelastic modulus of the cornea using optical coherence elastography, *Opt. Express* 27 (12) (2019) 16635–16649.
- [29] E. Leong, A. Aung, Weighted average velocity forward modelling of Rayleigh surface waves, *Soil Dyn. Earthquake Eng.* 43 (2012) 218–228.
- [30] K.D. Mohan, A.L. Oldenburg, Elastography of soft materials and tissues by holographic imaging of surface acoustic waves, *Opt. Express* 20 (17) (2012) 18887–18897.
- [31] D. Schneider, T. Schwarz, B. Schultrich, Determination of elastic modulus and thickness of surface layers by ultrasonic surface waves, *Thin. Solid. Films* 219 (1–2) (1992) 92–102.
- [32] L. Rayleigh, On waves propagated along the plane surface of an elastic solid, *Proc. Lond. Math. Soc.* 1 (1) (1885) 4–11.
- [33] G.-Y. Li, G. Xu, Y. Zheng, Y. Cao, Non-leaky modes and bandgaps of surface acoustic waves in wrinkled stiff-film/compliant-substrate bilayers, *J. Mech. Phys. Solids* 112 (2018) 239–252.
- [34] J.J. Pitre Jr, M.A. Kirby, L. Gao, D.S. Li, T. Shen, R.K. Wang, M. O'Donnell, I. Pelivanov, Super-shear evanescent waves for non-contact elastography of soft tissues, *Appl. Phys. Lett.* 115 (8) (2019) 083701.
- [35] G.-Y. Li, X. Feng, A. Ramier, S.-H. Yun, arXiv preprint, 2021.
- [36] A. Ramier, J.T. Cheng, M.E. Ravicz, J.J. Rosowski, S.-H. Yun, Mapping the phase and amplitude of ossicular chain motion using sound-synchronous optical coherence vibrography, *Biomed. Opt. Express* 9 (11) (2018) 5489–5502.
- [37] P. Lai, X. Xu, L.V. Wang, Dependence of optical scattering from Intralipid in gelatin-gel based tissue-mimicking phantoms on mixing temperature and time, *J. Biomed. Opt.* 19 (3) (2014) 035002.
- [38] J. Jachowicz, R. McMullen, D. Pretpypaul, Indentometric analysis of in vivo skin and comparison with artificial skin models, *Skin Res. Technol.* 13 (3) (2007) 299–309.
- [39] C. Li, G. Guan, Z. Huang, R.K. Wang, G. Nabi, Full skin quantitative optical coherence elastography achieved by combining vibration and surface acoustic wave methods, *Dynamics and Fluctuations in Biomedical Photonics XII, Int. Soc. Optics Photonics* (2015) 932200.
- [40] A. Pissarenko, W. Yang, H. Quan, K.A. Brown, A. Williams, W.G. Proud, M.A. Meyers, Tensile behavior and structural characterization of pig dermis, *Acta Biomater.* 86 (2019) 77–95.
- [41] C.T. McKee, J.A. Last, P. Russell, C.J. Murphy, Indentation versus tensile measurements of Young's modulus for soft biological tissues, *Tissue Eng. Part B: Rev.* 17 (3) (2011) 155–164.
- [42] M. Geerlings, L. Van Breemen, G. Peters, P. Ackermans, F. Baaijens, C. Oomens, In vitro indentation to determine the mechanical properties of epidermis, *J. Biomech.* 44 (6) (2011) 1176–1181.
- [43] A. Samani, J. Zubovits, D. Plewes, Elastic moduli of normal and pathological human breast tissues: an inversion-technique-based investigation of 169 samples, *Phys. Med. Biol.* 52 (6) (2007) 1565.
- [44] A. Park, Rheology of stratum corneum-II: a physico-chemical investigation of factors influencing the water content of the corneum, *J. Soc. Cosmet.* 23 (1972) 13–21.
- [45] M. Egawa, T. Hirao, M. Takahashi, In vivo estimation of stratum corneum thickness from water concentration profiles obtained with Raman spectroscopy, *Acta Derm. Venereol.* 87 (1) (2007) 4–8.
- [46] K. Parker, T. Szabo, S. Holm, Towards a consensus on rheological models for elastography in soft tissues, *Phys. Med. Biol.* 64 (21) (2019) 215012.
- [47] R.O. Potts, D.A. Chrisman Jr, E.M. Buras Jr, The dynamic mechanical properties of human skin in vivo, *J. Biomech.* 16 (6) (1983) 365–372.
- [48] F.H. Silver, J.W. Freeman, D. DeVore, Viscoelastic properties of human skin and processed dermis, *Skin Res. Technol.* 7 (1) (2001) 18–23.
- [49] Y. Pan, L. Gao, T. Bohlen, High-resolution characterization of near-surface structures by surface-wave inversions: from dispersion curve to full waveform, *Surv. Geophys.* 40 (2) (2019) 167–195.
- [50] C. Flynn, A. Taberner, P. Nielsen, Mechanical characterisation of in vivo human skin using a 3D force-sensitive micro-robot and finite element analysis, *Biomech. Model. Mechanobiol.* 10 (1) (2011) 27–38.
- [51] J.E.M. Manschot, A. Brakkee, The measurement and modelling of the mechanical properties of human skin in vivo—I. the measurement, *J. Biomech.* 19 (7) (1986) 511–515.
- [52] A.K. Dąbrowska, C. Adlhart, F. Spano, G.-M. Rotaru, S. Derler, L. Zhai, N.D. Spencer, R.M. Rossi, In vivo confirmation of hydration-induced changes in human-skin thickness, roughness and interaction with the environment, *Biointerphases* 11 (3) (2016) 031015.
- [53] A. Pons-Guiraud, Dry skin in dermatology: a complex physiopathology, *J. Eur. Acad. Dermatol. Venereol.* 21 (2007) 1–4.
- [54] T. Sugawara, K. Kikuchi, H. Tagami, S. Aiba, S. Sakai, Decreased lactate and potassium levels in natural moisturizing factor from the stratum corneum of mild atopic dermatitis patients are involved with the reduced hydration state, *J. Dermatol. Sci.* 66 (2) (2012) 154–159.
- [55] M. Lodén, Role of topical emollients and moisturizers in the treatment of dry skin barrier disorders, *Am. J. Clin. Dermatol.* 4 (11) (2003) 771–788.
- [56] X. Zhang, T.G. Osborn, M.R. Pittelkow, B. Qiang, R.R. Kinnick, J.F. Greenleaf, Quantitative assessment of scleroderma by surface wave technique, *Med. Eng. Phys.* 33 (1) (2011) 31–37.
- [57] G. Boyer, L. Laquière, A. Le Bot, S. Laquière, H. Zahouani, Dynamic indentation on human skin in vivo: ageing effects, *Skin Res. Technol.* 15 (1) (2009) 55–67.
- [58] F. Hendriks, D.v. Brokken, J. Van Eemeren, C. Oomens, F. Baaijens, J. Horsten, A numerical-experimental method to characterize the non-linear mechanical behaviour of human skin, *Skin Res. Technol.* 9 (3) (2003) 274–283.
- [59] R. Sanders, Torsional elasticity of human skin in vivo, *Pflügers Archiv* 342 (3) (1973) 255–260.

Supplementary Information

***In vivo* stiffness measurement of epidermis, dermis, and hypodermis using  
broadband Rayleigh-wave optical coherence elastography**

Xu Feng,<sup>a,c,1</sup> Guo-Yang Li,<sup>a,c,1</sup> Antoine Ramier,<sup>a,b</sup> Amira M. Eltony,<sup>a,c</sup> and Seok-Hyun Yun,<sup>a,b,c,\*</sup>

<sup>a</sup> Harvard Medical School and Wellman Center for Photomedicine, Massachusetts General Hospital,  
Boston, Massachusetts 02114, USA

<sup>b</sup> Harvard-MIT Division of Health Sciences and Technology, Cambridge, Massachusetts 02139, USA

<sup>c</sup> Department of Dermatology, Massachusetts General Hospital, Boston, Massachusetts 02114, USA

<sup>1</sup> Co-first authors with equal contribution.

\* syun@hms.harvard.edu

## S1. Finite element analysis

We built a plane strain model to study the wave propagation in the three-layer model. As shown in Fig. S1a, the width of the model is denoted by  $w$ . We scaled the size of the model using the wavelength  $\lambda$ , i.e.,  $w = 15 \lambda$ . The thickness of the third (hypodermis) layer  $h_H = 0.5w$ , which is large enough to avoid the reflections from the bottom. A time-harmonic pressure  $p(t)$  with a Gaussian distribution (radius  $\sim 0.1 \lambda$ ) was applied on the surface to excite the wave propagation. We used a symmetric boundary condition on the left side of the model. Other boundaries were stress free. The element type used in this study was 8-node biquadratic element (CPE8RH). Since only the surface wave motion was interested, we adopted a gradient mesh (Fig. S1b) to reduce the computation cost. The minimum size of the element was  $\sim 0.02 \lambda$ .

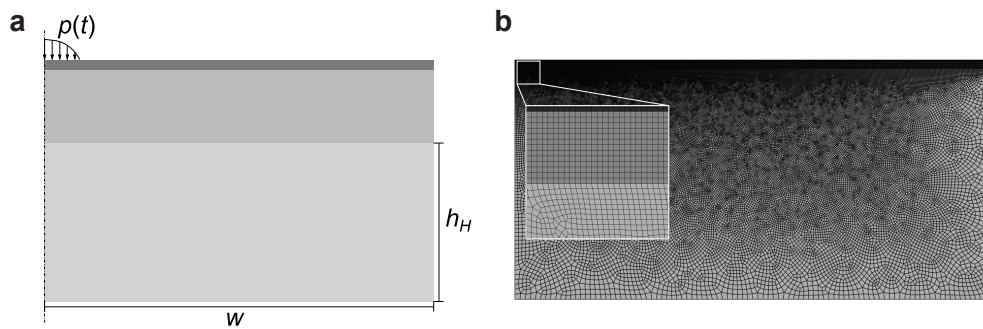


**Fig. S1.** Finite element analysis. (a) Boundary conditions and loads. (b) A representative mesh of the finite element model.

## S2. Mechanical characterization of the phantoms

Figure S2 displays the raw data used for estimating the reference Young's moduli of the individual phantom layers in Table 1. Figure S2 (a) shows the phase velocity dispersion curve of the PDMS film (thickness  $150 \mu\text{m}$ ) and the fitting curve with a Lamb wave model [1]. The estimated shear wave velocity was  $19.7 \pm 0.7 \text{ m/s}$ . Figure S2 (b) shows the dispersion curve of the bulk gelatin phantoms ( $35 \text{ mm}$  in diameter and  $10 \text{ mm}$  in height). The Rayleigh-type elastic wave speed  $v_R$  was determined from the average wave speed in the range of 1 to 10 kHz. The shear wave velocity is then determined as  $v_S = v_R/0.955$  [2]. The measured shear wave velocity of the 7% and 3% bulk gelatin phantom were  $3.0 \pm 0.1 \text{ m/s}$  and  $1.7 \pm 0.1 \text{ m/s}$ , respectively. The Young's modulus is then given by  $E = 3\rho v_S^2$ , where  $\rho$  is the density ( $\rho = 965 \text{ kg/m}^3$  for PDMS and  $1000 \text{ kg/m}^3$  for gelatin). We have determined that Young's modulus of the PDMS film is  $1.13 \pm 0.08 \text{ MPa}$ , 7% gelatin phantom has  $27 \pm 2 \text{ kPa}$ , and 3% gelatin phantom has  $9 \pm 1 \text{ kPa}$ .

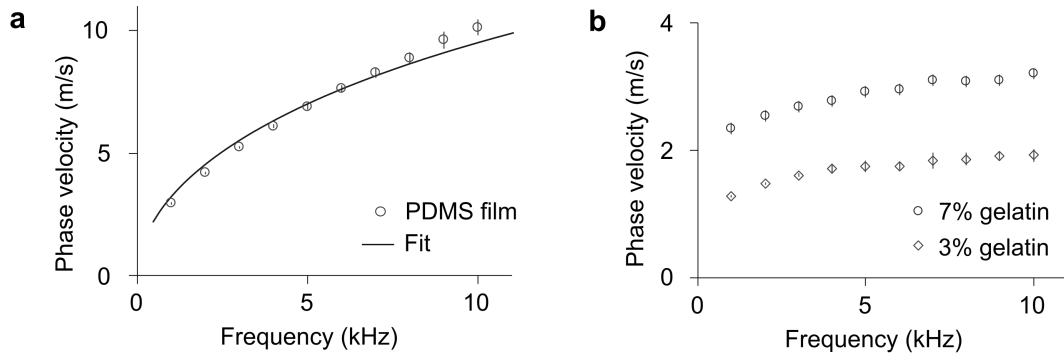


**Fig. S2.** Mechanical characterization of the materials used in the phantoms. (a) PDMS thin film. Measured dispersion curve (dot) is fitted by the Lamb wave model (solid line). (b) Measured phase velocity dispersion curve for the 7% gelatin phantom (dots) and the 3% gelatin phantom (diamonds). Error bars represent the standard deviation of three measurements at three different locations.

## References

1. A. Ramier, B. Tavakol, and S.-H. Yun, "Measuring mechanical wave speed, dispersion, and viscoelastic modulus of the cornea using optical coherence elastography," *Opt Express* **27**, 16635-16649 (2019).
2. A. Ramier, A. M. Eltony, Y. Chen, F. Clouser, J. S. Birkenfeld, A. Watts, and S.-H. Yun, "In vivo measurement of shear modulus of the human cornea using optical coherence elastography," *Scientific reports* **10**, 1-10 (2020).

### S3. Tip-induced displacement amplitude at all frequencies

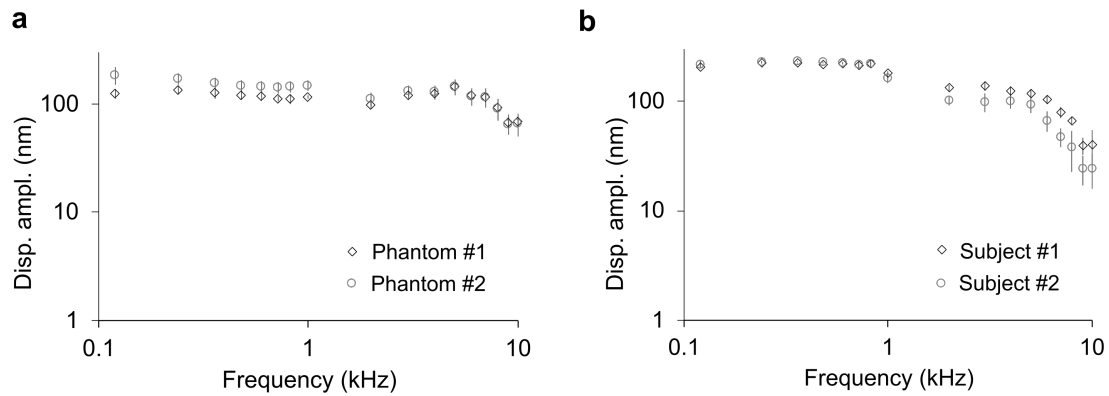


**Fig. S3.** The displacement amplitudes of the elastic waves near the tip in the phantom samples and skin tissues. (a) Skin-mimicking phantom #1 (diamond) and phantom #2 (dot). The displacement amplitude at 10 kHz is greater than 50 nm for all measurements. (b). Forearm skin of subject #1 (diamond) and subject #2 (dot). The displacement amplitude at 10 kHz is  $\sim 30$  nm for subject #1 and  $\sim 20$  nm for subject #2. Error bars represent the standard deviation of three measurements.

#### S4. Dimensionless root-mean-square-error (RMSE) values in fitting

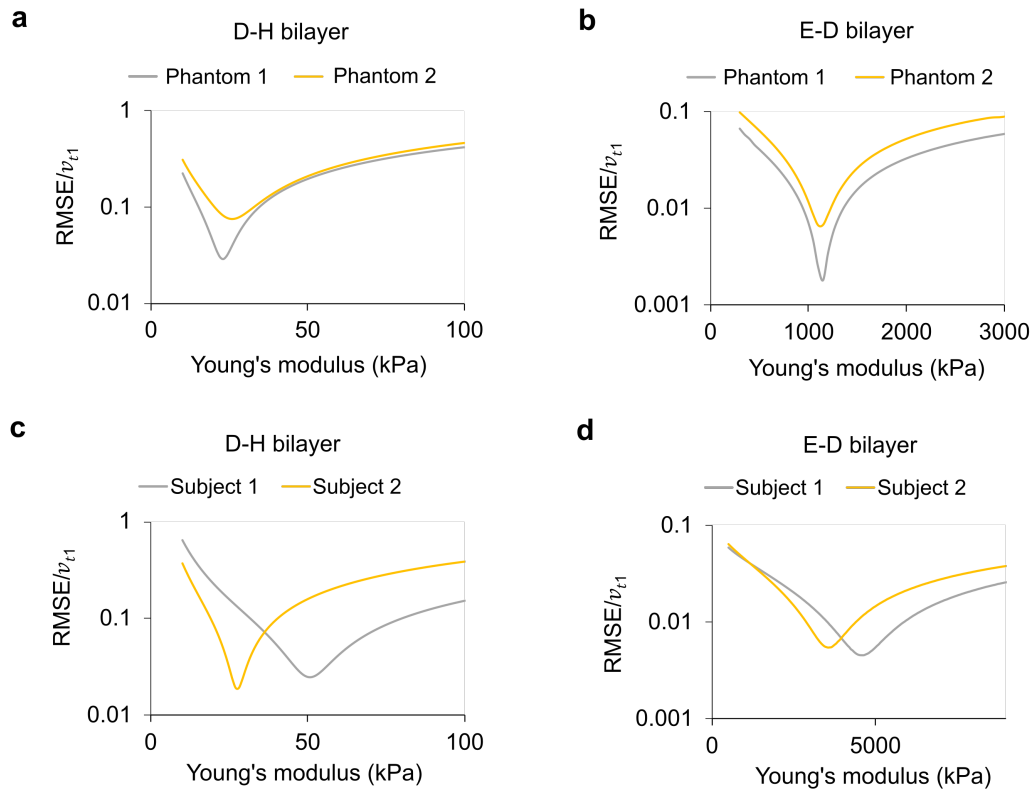


**Fig. S4.** The dimensionless RMSE with the fitting parameter  $v_{1t}$  for (a) D-H bilayer, phantom. (b) E-D bilayer, phantom. (c) D-H bilayer, forearm skin. (d) E-D bilayer, forearm skin.  $v_{ti}$  is the estimated transverse wave speed of the top layer (for the D-H bilayer the top layer refers to the dermis, while for the E-D bilayer the top layer refers to the epidermis). For all models, there is only one optimum fit that minimizes the RMSE.

## S5. Comparison between finite element analysis and experimental data of human subjects

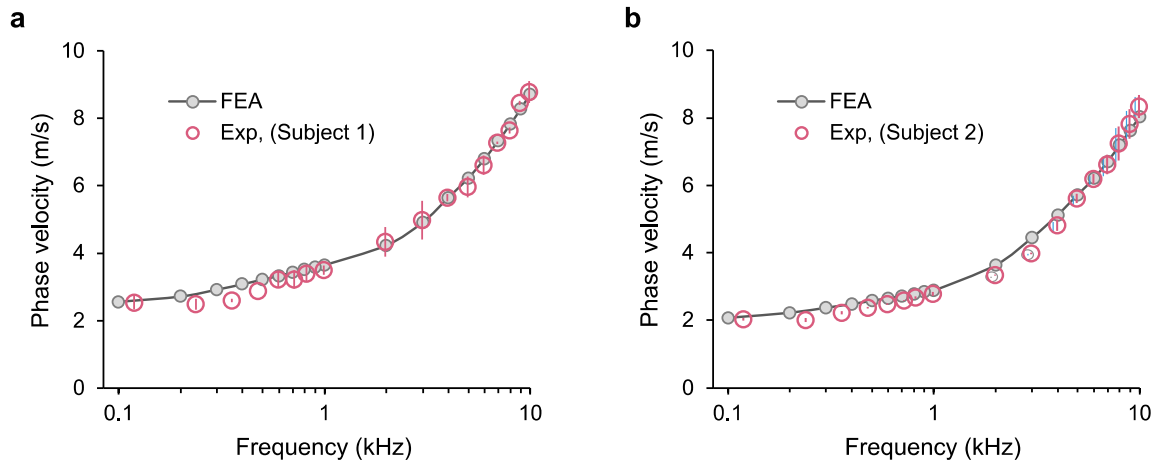


**Fig. S5.** Comparisons between the finite element analyses (FEA) and experimental data. (a) Subject #1 and (b) Subject #2. The FEA results were obtained using the fitting parameters in Table 3 in the main text.

**S6. Effect of viscoelasticity in fitting**

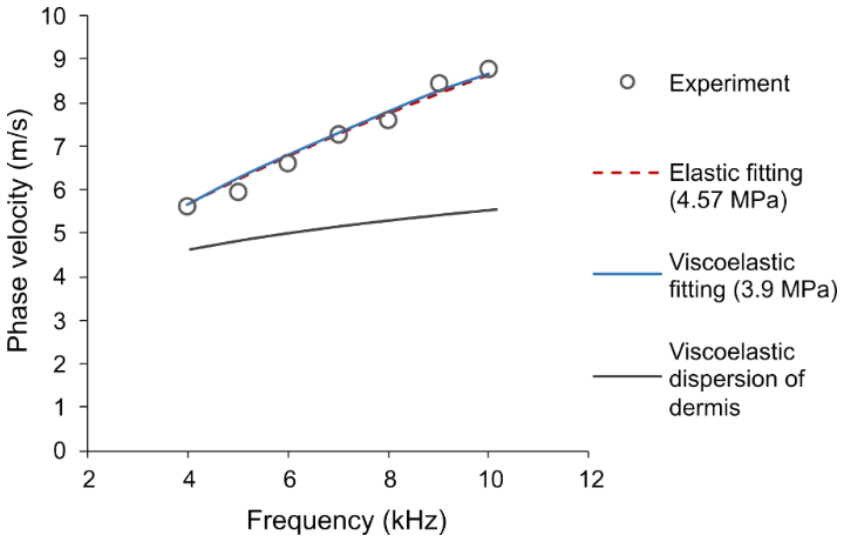


**Fig. S6.** Effect of the viscoelasticity of the dermis on the fitting result. Dots: experimental data from Subject #1. Solid black line: the viscoelasticity of the dermis obtained from the power law model. Dashed red line: fitting with an elastic model. Solid blue line: fitting with a viscoelastic model.